

In situ SEM-EBSD analysis of plastic deformation mechanisms in neutron-irradiated austenitic steel

M. N. Gussey, K. J. Leonard

Abstract

In situ tensile tests, accompanied by scanning electron microscopy coupled with electron backscatter diffraction (EBSD) analysis were performed on neutron-irradiated 304L steel specimens (5.9 dpa, irradiation in boiling water reactor at 288°C). Selected regions of interest were analyzed following tensile deformation of the specimens to increasing levels of strain, allowing for tracking and investigating strain-induced misorientation evolution, lattice rotation, twinning, and phase instability. Deformation-induced changes in EBSD misorientation parameters, such as kernel average misorientation (KAM) and grain reference orientation deviation (GROD), were analyzed as a function of the strain level (ϵ). The mapping of GROD values revealed the formation of specific “hot spots” (areas with high local misorientation) in the early stages of tensile deformation ($\epsilon \sim 0-0.02$) with values increasing much more quickly for irradiated specimens than for nonirradiated specimens. In contrast, average KAM values showed very little change in the small strain range ($\epsilon < 0.02$) and fast growth at larger strain values.

Keywords: Irradiated austenitic steels, in situ tensile testing, localized deformation, kernel average misorientation (KAM); grain reference orientation deviation (GROD).

1. Introduction

Electron backscatter diffraction (EBSD) coupled with scanning electron microscopy (SEM) is a powerful research technique for studying material structure and evaluating plastic deformation processes [1–9]. EBSD has excellent flexibility regarding magnification level and resolution and uses sophisticated postprocessing algorithms [10,11] to describe crystal misorientations and microstructure features [1,3,4]. An analysis of the literature [1,2,4,9] showed that there is a close connection between lattice misorientation parameters and plastic strain or mechanical damage level. Numerous EBSD misorientation parameters were offered and evaluated to quantify strain-induced changes in the structure: kernel average misorientation (KAM) [12], grain average misorientation (GAM) [2], and grain reference orientation deviation (GROD), to name a few. These parameters, being averaged for some area, correlate well with the degree of plastic strain [2,12–15], fatigue life fraction [16,17], and creep [18–20].

The magnitude and density of the microstructure defects accumulated by a material during a deformation test or while in service may be quantified using a correlation curve connecting the selected EBSD misorientation parameter (e.g., KAM average value) and a degree of the damage or strain level (ϵ) [2,4,5,8]. Such correlation curves may be independent to a particular EBSD system [4], and once the correlation curve is constructed, for instance via controlled deformation tests, the degree of strain level of an unknown object may be reliably quantified. Quantification of changes in structure is especially important for evaluating nuclear power plant (NPP) components that experience extended service life conditions. Plastic strain and localized deformation of an NPP component may compromise its performance. For instance, dislocation channels may precede crack initiation [21], and localized deformation (e.g., deformation bands, “hot spots” [22]) may form preferable sites for corrosion [23]; however, very limited data exist on EBSD micro-structure evaluation of ex-service NPP components.

EBSD is often used in conjunction with in situ mechanical testing (i.e., continuous or step-by-step loading, plastic deformation, or fatigue testing) [24–30] to investigate stress- and strain-induced phenomena. In this case, a single irradiated (and thus valuable) specimen may provide results for a broad range of stress and strain levels [31]; a selected area may be reliably evaluated, revealing strain-induced changes in great detail. Whereas EBSD is widely employed to investigate irradiated metals and alloys [32–36], published results on characterizing and quantifying strain-induced phenomena after irradiation are sparse. The radiation-induced damage in metallic materials changes deformation modes, initiating deformation localization and channeling [1,7,32,37,38]. Therefore, the changes in acting deformation mechanisms in irradiated materials will put under question the reliability of the EBSD correlation curves [e.g., average KAM(ϵ)] obtained for unirradiated specimens of the same material. To address this knowledge gap, in situ mechanical tests, accompanying by SEM-EBSD scanning were performed with neutron-irradiated and nonirradiated 304L steel specimens. This work provides a

necessary step in evaluating the interconnection between strain localization and crack initiation and attempts to define characterization parameters by which materials can be assessed. EBSD misorientation parameters obtained from in situ testing were analyzed for the selected regions of interest (ROIs) scanned at different strain levels. Relationships connecting strain level and EBSD misorientation metrics were established for the irradiated material.

2. Experimental method and studied material

2.1. Investigated material

Nuclear-grade AISI 304L austenitic stainless steel irradiated in a commercial reactor (Barsebäck 1 boiling water reactor, Sweden) was selected for this study (Table 1). The material, provided by Studsvik Nuclear AB, was cut from a control rod blade. The control rod was in operation for 95,608 h with an accumulated neutron damage dose of 5.9 dpa [39]. The material had relatively high nickel content and a grain size of ~ 55 to $60 \mu\text{m}$; details on the irradiated material microstructure may be found in [40]. Magnetic measurements with an industrial ferroprobe unit revealed a small amount of magnetic phase ($< 0.2\%$); metallographic examination showed an almost fully austenitic structure with small, sparse ferrite inclusions, in most cases less than 3 to $5 \mu\text{m}$.

Nonirradiated archive material from the same heat was not available; thus, a small substitute heat was produced to provide the baseline for comparison. The substitute heat [22] had an element composition and grain size (Table 1) close to the irradiated material but contained no ferrite.

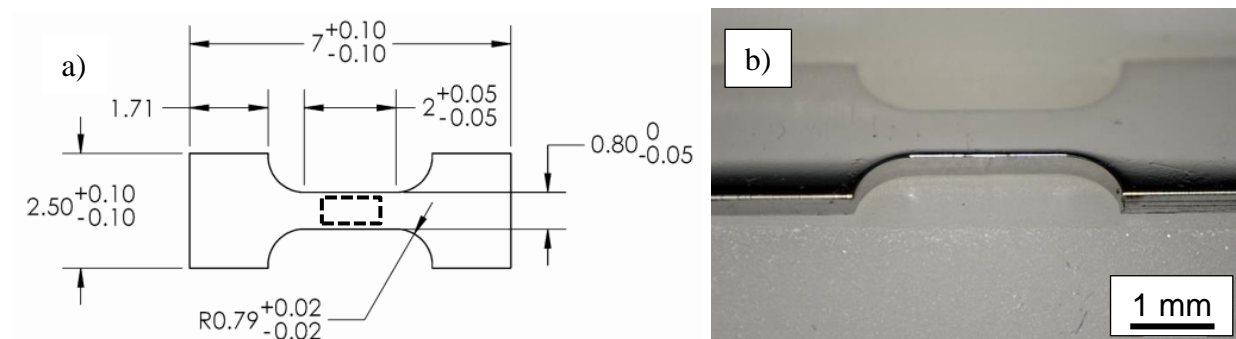


Figure 1. Geometry, dimensions (a), and a general view (b) of the tensile specimen for in situ testing (thickness was $\sim 0.35 \text{ mm}$). The surface quality of the specimen was suitable for EBSD. The scans were performed on the specimen flat side (dashed rectangle).

Irradiated tensile specimens (Figure 1) were manufactured at Oak Ridge National Laboratory (ORNL) using a computer numerical control milling machine located in the Low Activation Materials Development and Analysis Laboratory (LAMDA). Nonirradiated tensile specimens were produced by a commercial vendor using an electric discharge machine. The flat sides of all

specimen blanks, both irradiated and nonirradiated, were polished using 3 μm diamond lapping paper and then were electropolished for 10 s at 30 V DC using Struers A2 electropolishing solution. After preparation, the specimens had a mirror-like clean surface, suitable for EBSD analysis, and a thickness of $\sim 350 \mu\text{m}$. The specimen geometry was designed to have a small gauge portion. Preliminary tests with the cold-worked 316L steel showed that a neck will form close to the middle of a specimen and will occupy most of the gauge section, thus minimizing the number of reference EBSD scans required to cover the gauge section. Whereas this geometry (Figure 1) provided a tensile stress state during the in situ mechanical test, it was not designed to deliver the mechanical property values comparable to other miniature [41] or standard specimens. The yield stress values were comparable to massive specimens, but ductility values may vary due to the short gauge used.

Table 1. Composition (wt %) and grain size for the 5.9 dpa irradiated steel and reference material

Internal material code	Description	Dose, dpa	Fe	C	Mn	Si	Cr	Ni	Mo	N	Grain size (μm)
SW2	Nuclear-grade, 304L steel	5.9	Bal.	0.025	1.09	0.30	18.35	10.57	n/d	0.024	55–60
SW'	Reference	–	Bal.	0.016	1.03	0.24	18.39	10.45	0.0013	0.056	57

2.2. SEM-EBSD in situ tensile testing

In situ mechanical testing was conducted using an FEI VERSA 3D SEM equipped with an Oxford Instruments Nordlys-2 EBSD system with maximum pattern size of 640 by 480 pixels. The voltage was fixed at 20 kV, and nominal beam current values were 8 nA or 32 nA. The beam current of 32 nA was employed to collect reference data prior to testing. The 8 nA beam current was used during the in situ tensile test once the yield stress point was reached. The reasons behind the beam current variations are discussed in [42]. The microscope was equipped with an MZ.Sb (Kammrath and Weiss Tech.) miniature tensile frame to perform the in situ mechanical testing. The tensile tests were conducted at a nominal strain rate of 10^{-3}s^{-1} at room temperature (RT). During the EBSD scans, the load was slightly reduced to minimize creep-related effects; nevertheless, some ($\sim 10 \text{ N}$) additional relaxation (load decrease between the steps) was usually observed. EBSD data collected during the in situ test were processed using EDAX OIM v.7.2 software. The data was imported from Oxford AZtec software with careful attention to the Euler angle change convention between these two vendors. EDAX OIM was used to calculate KAM and GROD values and maps. KAM was selected as a typical kernel-based misorientation parameter [9], and GROD represented a grain-based [9] misorientation metric. The KAM is the average misorientation angle of a given point with all its neighbors. Here, KAM was calculated using only the nearest neighbors (1 step or 1st order KAM), maximum misorientation of 5° , and using all points in the kernel. GROD is a grain-based

misorientation parameter; in the present work, to get the GROD value, the average orientation for the grain was calculated first. After that, the GROD for each point within the grain was calculated as a difference between this point orientation and the average orientation of the given grain.

EBSD settings (e.g., working distance, binning, magnification) were kept as consistent as possible for the irradiated and reference specimens through the test. Selected ROIs (four per irradiated tensile specimen) with initial dimensions of $150 \times 150 \mu\text{m}$ were scanned with a step (pitch) of $0.5 \mu\text{m}$ at $650\times$ magnification (which corresponds to a horizontal field of view of $\sim 315 \mu\text{m}$) and using 2×2 binning. Several subareas with features of interest were additionally scanned at $2,000$ to $2,500\times$ with a 125 nm step. The correct identification of strain-induced features (e.g., twins, ferritic grains, martensitic domains) was verified through separate analysis of the recorded Kikuchi patterns, by analogy with [43]. Misorientation angle of 5° was selected to identify grains in the EBSD scans. Compromises were made regarding the numbers of ROIs, their sizes, EBSD resolution or step size, and the number of deformation steps so that the necessary statistics could be obtained in the time available at the instrument.

During the in situ experiment, local strain values at the surface might have been different from an externally applied nominal strain (often termed as “global strain” [44]). For irradiated austenitic steel, the difference is caused by earlier necking (nonuniform elongation) due to radiation-induced channel formation. To describe and quantify strain-induced processes, one has to operate by strain level at the given location, not by global strain. To measure the local strain level, the same specific points (e.g., inclusions in the SEM images or triple junction points in EBSD maps) were used as fiducial marks and were tracked through the datasets for all strain levels. The distance between the points, treated as a “virtual gauge,” was used to calculate the local strain levels [44]. To minimize the impact of SEM image distortion [45] on the results, SEM magnification was $650\times$. For each ROI, five to seven virtual gauges were evaluated, and an average strain value was reported in terms of the engineering definition of strain.

3. Experimental results

3.1. Mechanical behavior of the investigated materials

Figure 2 shows tensile curves obtained during in situ tests in comparison with the ex situ results; the ex situ tests were conducted with the same material and specimen geometry using a screw-driven electromechanical MTS tensile frame. The results for the irradiated specimens tested in situ and ex situ are very close. Nonirradiated specimens tested in situ demonstrated slightly higher strength; the observed difference ($\sim 8\%$ to 10%) may be explained by a natural scattering of the results for small thin specimens and by relaxation between steps, as is discussed below.

Note that the tensile frames used for ex- and in-situ testing, had different compliance, which also could contribute to the difference between the tensile curves in Figure 2.

The in situ tests were interrupted at the global strain levels of ~20% for the irradiated specimen, and at ~30% to 35% for nonirradiated specimens because strain-induced roughness led to the degradation of the EBSD dataset (e.g., the appearance of nonindexed areas as a result of shadowing of the detector due to surface morphology changes). At higher strains, the preselected ROIs lost integrity, making it difficult to track locations, grains, or objects with phenomena of interest.

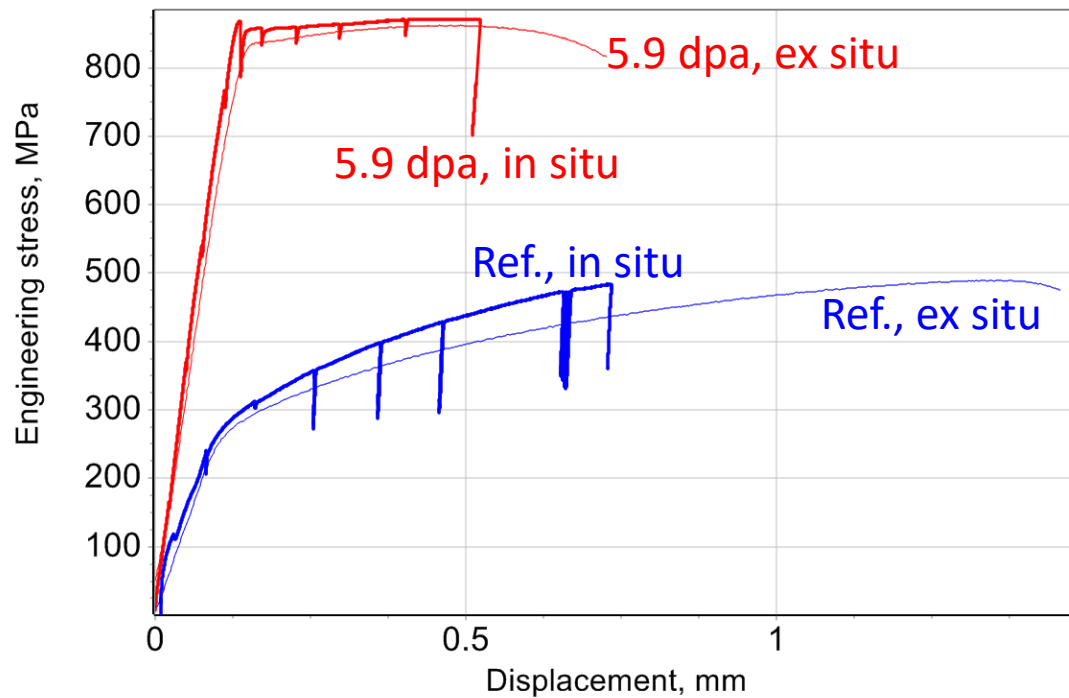


Figure 2. Tensile curves obtained for the ex situ tests (thin lines) and in situ tests (thick lines with unloading segments).

The in situ tensile curves had small unloading/relaxation segments caused by interruptions in the testing. Partial unloading was employed between the steps; nevertheless, it was impossible to fully eliminate relaxation. Test interruptions and stress relaxation cannot be considered as a fully neutral event. For instance, mechanical tests, conducted recently with nonirradiated 316 steel demonstrated that stress relaxation might improve ductility and delay neck formation [46] via a slight increase in the deformation hardening rate. The mechanism may depend on the strain level, strain rate, or the number and duration of the test interruptions. This phenomenon has not been fully investigated for irradiated materials under tensile stress; most previous work has been focused on the disappearance of loading stress under continuous irradiation [47]. As discussed in [46], the relaxation effects depend on the density of mobile dislocations, back stresses, and other

structural parameters. Strong deformation localization and dislocation channel formation in irradiated austenitic steels may lead to a different relaxation behavior compared with the behavior of nonirradiated materials. This aspect requires additional investigation in the future. In our work, no significant interruption-caused increase in the acting stress or load was observed during the reapplication of the load. In most cases, the tensile curve continued to follow the same trend smoothly and without pronounced changes in force.

3.2. Surface morphology evolution

Figure 3 shows the difference in the deformation mechanisms between nonirradiated and irradiated austenitic steels. Multiple fine slip lines are barely visible in the nonirradiated steel at 650 \times magnification (Figure 3a). At the larger magnification level (Figure 3b), the spacing between the slip lines and the individual height of the slip lines are both shown to be very small. Strain-induced roughness and surface morphology changes are clearly visible in the SEM images taken at 70 $^\circ$ tilt angle.

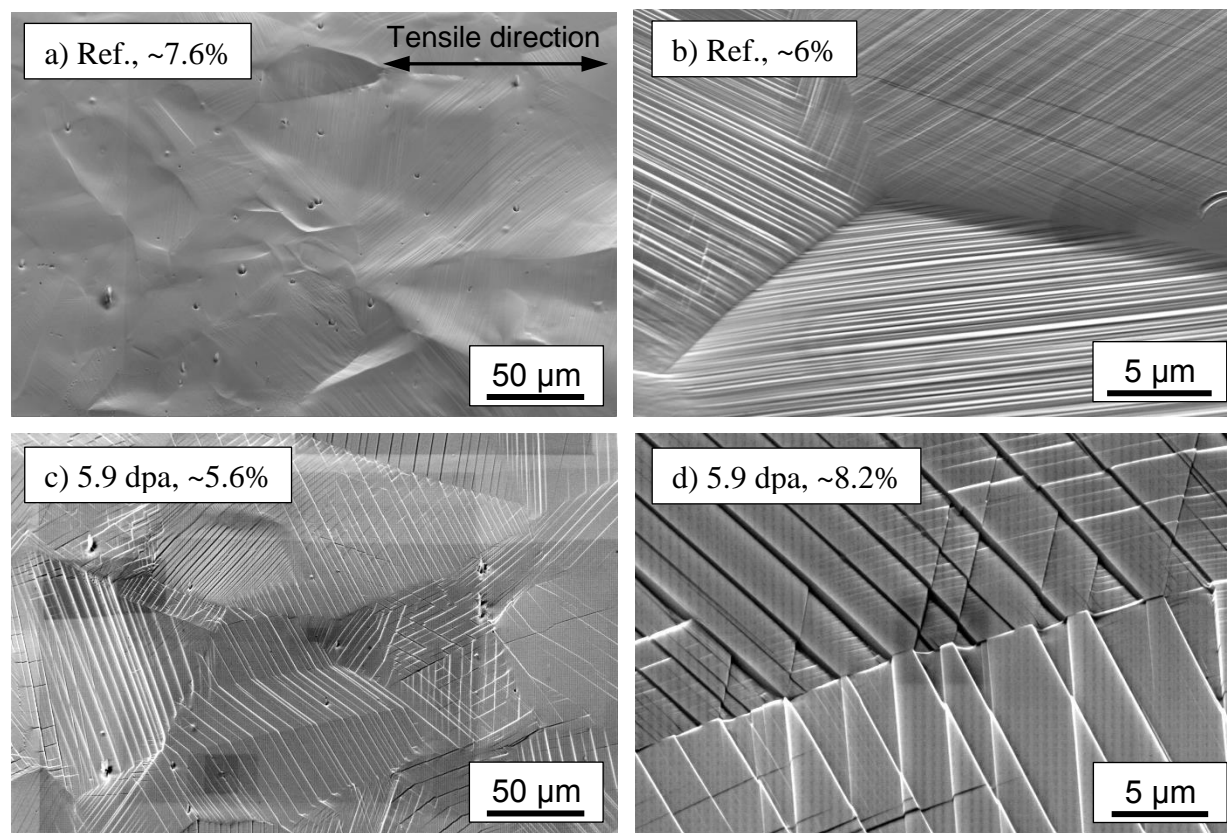


Figure 3. Surface morphology of the reference (a, b) and 5.9 dpa-irradiated (c, d) AISI 304L steel specimens after plastic deformation at room temperature. All images are taken at a 70 $^\circ$ specimen tilt angle. Strain values are given in the local strain terms. Left column: low-magnification images that provide a general view of the deformed area, right column: images taken at moderate magnification. Tensile direction (horizontal) is the same for all Figures in the paper.

Neutron irradiation and subsequent deformation drastically change surface morphology. Numerous fine slip lines, observed in the nonirradiated steel, are replaced by relatively coarse, defect-free channels (Figure 3c) in the irradiated steel [48,49]. Whereas multiple slip systems may operate in a single grain, one or two slip planes are usually dominant in a grain and lead to the formation of coarse slip lines and steps at the surface; however, multiple slip planes are often active in the vicinity of the grain boundary (Figure 3d). An exact number of active slip planes may be not easy to define. High tilt angle makes some slip lines difficult to see and plastic strain, in some rare cases, does not lead to the out-of-plane displacement.

The practical consequence of the channel formation is a strong tendency toward localized deformation [48,49]. Dislocation motion occurs mainly inside channels, in the thin, narrow areas free of radiation defects, whereas a significant fraction of material volume has limited, if any, dislocation activity. Inside the channels, pronounced dislocation pileups may form at relatively small strains, leading to high local stresses [50]. Interaction of the dislocation channels with grain boundaries may be complex [51], the worst outcome in a corrosive environment is crack initiation [51]. Crack initiation has also been observed during testing in argon at slow strain rates and at elevated temperatures [52].

Additionally, in situ tests allow for studying the slip transfer between grains and slip line – grain boundary interaction, as one may see in Figure 3. However, this aspect was out of the present work scope since it will require a different in situ test plan with much smaller strain increments. In the context of the present work, it is important that a structure with more or less uniform dislocation distribution within multiple fine slip lines (Figure 3b) will be replaced by a structure with sharp fluctuations in the dislocation density. This change in the deformation modes, which has been widely investigated using transmission electron microscopy (TEM) [53] and theoretical modeling [38,54,55], and, to a limited extent, in situ testing [56], may have a strong impact on EBSD-defined strain metrics.

3.3. EBSD dataset analysis

Figure 4 shows an EBSD dataset recorded at different local strain levels for a typical ROI. The dataset includes an inverse pole figure (IPF) map (sometimes termed as map of crystal orientations with IPF coloring), showing grain structure and reflecting grain orientation regarding some selected direction (tensile direction in the present work), an image quality (IQ) map, and two maps with common EBSD parameters describing misorientation in the microstructure (GROD and KAM). Figure 5 provides additional statistics and insight for nonirradiated (Figure 5a) and irradiated (Figure 5b) specimens at a comparable strain level. A number of other EBSD misorientation parameters, such as grain average misorientation [2] or modified crystal deformation [5] may be used as well [2,5] but are not discussed in the present work. Two particular EBSD misorientation parameters – GROD and KAM – were selected since

the first is grain-based (i.e., the whole grain is used to evaluate GROD) and the second is kernel-based allowing for evaluating local changes in material structure.

3.3.1. IQ Maps

In the conventional post-test EBSD analysis, the IQ value is a quantitative indicator of the EBSD pattern quality and may also be a qualitative indicator of the presence and density of defects (e.g., grain boundary, slip line, strain-induced dislocations) [57]. EBSD software usually represents IQ as a value from 0 (the worst) to 1 (the best) or between 0 and 255 (or some other maximum value). Regarding the in situ test, the IQ values may also be affected by surface steps or by surface rotation. The IQ maps, taken at different strain steps, are useful as an indication of strain-induced processes and changes in the structure and should be analyzed with other maps or SEM images.

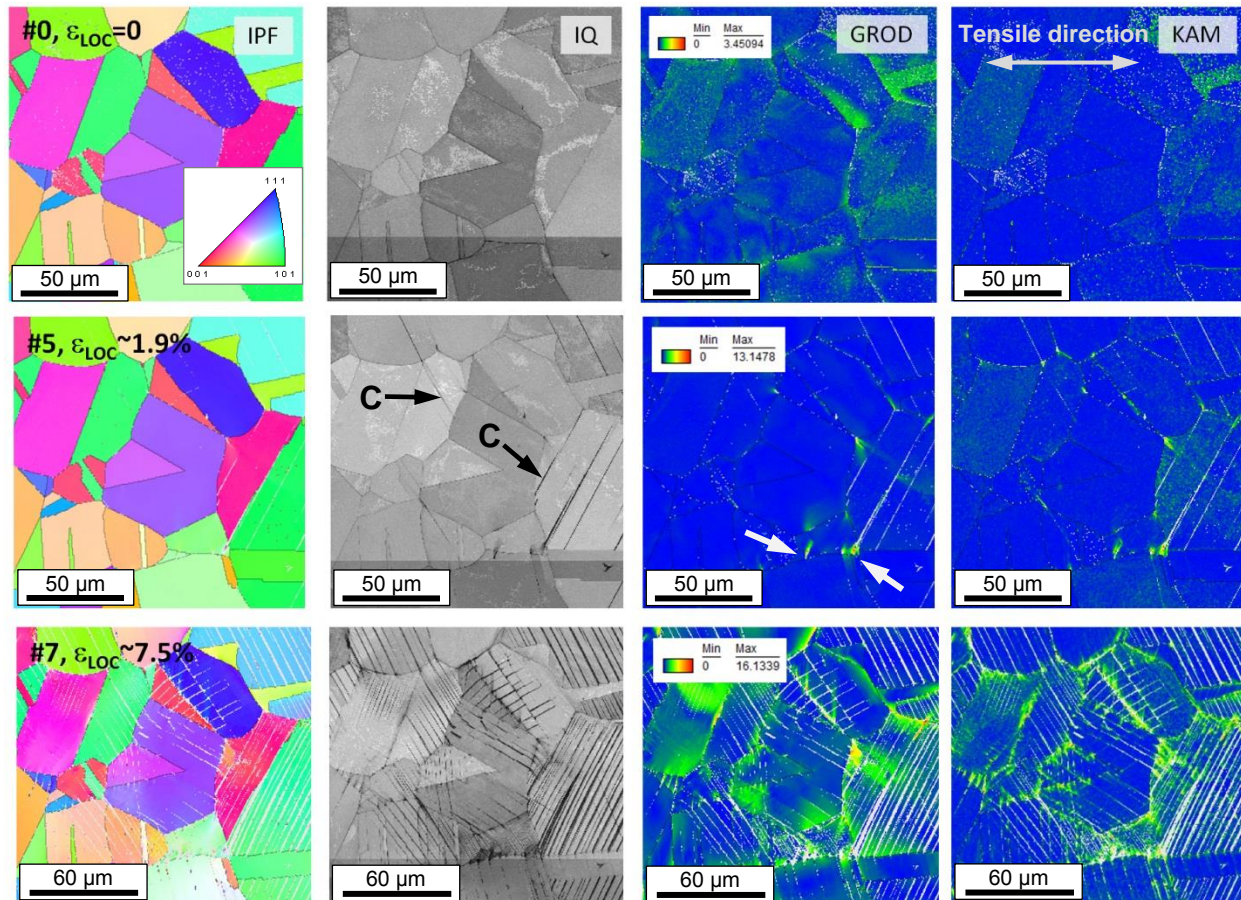


Figure 4. Typical EBSD dataset obtained during the in situ SEM-EBSD test: (left to right) IPF map (maps of crystal orientation with IPF coloring), IQ, GROD, and KAM maps. Black arrows point to dislocation channels (C). White arrows in the GROD maps indicate spots with high local deformation. IPF maps are colored with respect to the tensile direction. The IPF key is the same for all IPF maps in the paper.

For irradiated and deformed austenitic steels, strain-induced changes at small strains are clearly visible in IQ maps [43,58] (Figure 4). When the reference image is compared with the post-deformation IQ maps, the dislocation channels appear as dark lines with reduced IQ that indicate degradation of EBSD pattern quality. Reductions in IQ value are caused, in part, by surface roughness and step formation in the strained material and by increased dislocation density inside the channel. Even in highly polished, mirror-like surfaces, dislocation channels appear as dark lines in IQ maps [33]. Additionally, the IQ values indicate an increase in the local defect density due to local plastic deformation. Defect-induced changes in IQ usually coexist with changes in KAM and GROD parameters, as is discussed below.

3.3.2. GROD maps

The GROD misorientation metric provides a misorientation map referenced to a mean orientation of all points belonging to a grain. The GROD parameter defines how a given point in a grain is bent or rotated in reference to the mean orientation of the entire grain. The GROD parameter is often used in quantifying the recrystallization process to separate deformed and recrystallized grain populations [59,60]. This is due to the recrystallized, strain-free grains having smaller GROD values. Also, GROD maps are especially useful for highlighting localized changes in the material structure. For example, laser-induced ablation of material produces an impact wave that introduces high local density of dislocations in the near surface layer of ~ 200 nm thickness [61].

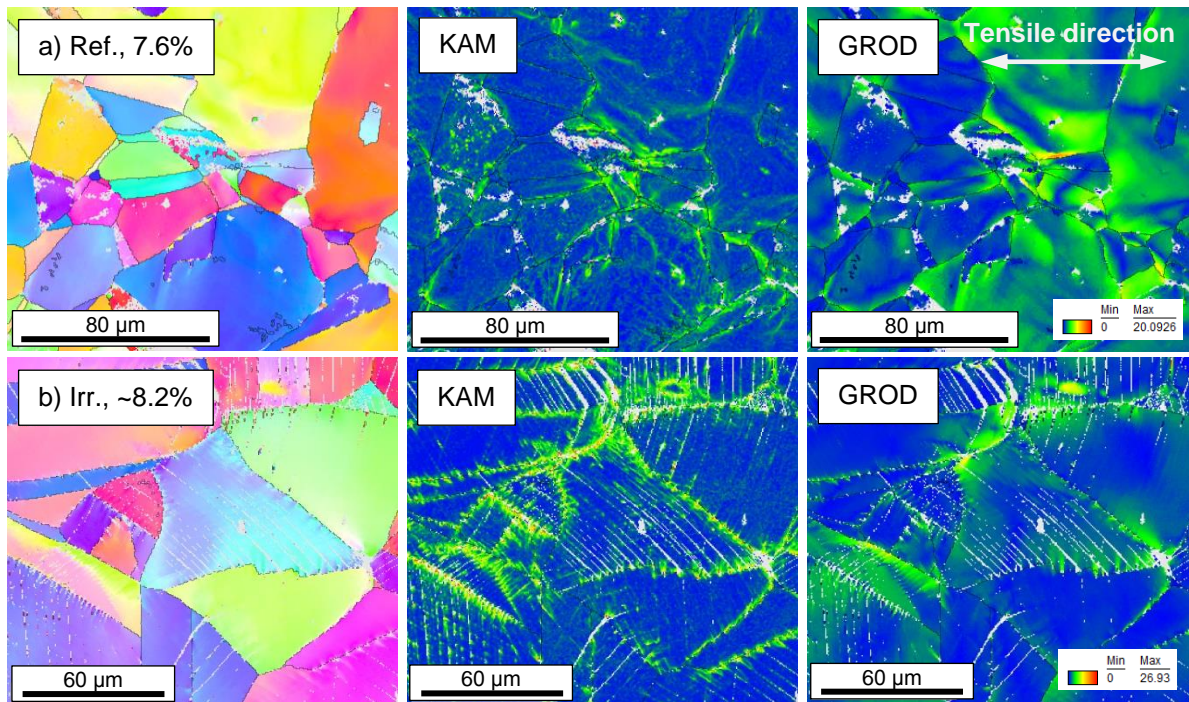


Figure 5. IPF, KAM, and GROD maps for nonirradiated (a) and irradiated (b) steel specimens at a comparable strain level ($\sim 8\%$).

For data analyzed in the present work, weak GROD variations, usually below the range of 1° to 1.5° , may be seen within grains in the nondeformed material (Figure 4). These variations show the presence of a dislocation substructure after material fabrication or indicate in-service defect accumulation.

Local GROD value may increase suddenly when plastic deformation occurs in irradiated austenitic steel (Figure 4, white arrows). The GROD map for the 1.9%-strained area (Figure 4) showed specific spots, or areas with high local misorientation, formed either at channel/grain boundary interaction points or near triple junction points. The GROD values for that ROI were observed to be as high as $\sim 13^\circ$, and misorientation gradients near those locations reached up to a few degrees per micron. For this case – at small strain levels of the irradiated steel specimen – such strong local misorientation values reflect high local fluctuations in dislocation density, where small deformed areas coexist within a practically nondeformed portion of the grain.

Such local formations were observed earlier [22] and were termed “hot spots.” An extreme case was measured using a focused ion beam (FIB)-TEM approach as an increase in GROD value up to 23° after the plastic strain of 0.8% in a bend specimen of 304L steel irradiated to 4.4 dpa. Within an area of only 3 to 4 μm , multiple fine channels, a high local density of dislocations, twinning, and a phase transformation developed due to straining were observed [22]. Interaction of slip lines (defect-free channels) with grain boundaries often forms “dislocation blooms” in areas adjacent to the grain boundary. The areas with high local defect density (deformation bands) may compromise material performance in aggressive environments such as liquid metals [23]. Also, in comparisons of the GROD maps for nonirradiated and irradiated steels (Figure 5), local GROD variations in the irradiated specimen are often observed near grain boundary, whereas the GROD gradients occur across the whole grain in the nonirradiated material.

Thus, mapping the GROD value is a convenient way to highlight the localized deformation in irradiated austenitic steel specimens deformed at the small plastic strain. EBSD scanning should be performed with relatively small step size (0.5 μm or less) for the hot spots to be reliably observed. If a coarse step size ($\sim 2\text{-}4 \mu\text{m}$) is used, the hot spots may appear as separate very small grains, and, most likely, will be dismissed during data analysis.

As local strain increases, GROD in the irradiated steel specimen usually continues to increase but at the much slower rate. At a moderate strain level (see an example in Figure 4), the GROD values changed smoothly inside grains and revealed mostly lattice rotation or bending.

3.3.3. KAM maps

The KAM values characterize changes in the local misorientation caused by geometrically necessary dislocations [4]. KAM plotted as a map reveals areas with an increased density of the defects, and as an average value for the whole scan, may reflect material strain history [4].

Regarding the dataset shown in Figure 4, the KAM map for the nondeformed irradiated material does not exhibit any significant gradients inside grains, showing the material was practically strain-free. At small strain levels applied to the specimen, the increased KAM values usually coincide with a GROD hot spot. However, increased KAM values are often observed along grain boundaries, indicating the formation of fine channels or slip lines at different locations.

At moderate (5%–8%) strains, high-KAM locations in irradiated steel usually exist at the channel-grain boundary intersections. Their existence is indicative of increased local dislocation density and dislocation pileup formation (Figure 5). Sometimes high KAM values may be observed along the dislocation channel, suggesting the presence of dislocations inside the channel. However, some grains with rough channels may have very small, if any, increase in the KAM value within a grain body, far from the grain boundary. Dislocation channel intersections within a grain body, which may also be visible in the KAM map most likely indicate the presence of dislocation debris. Joint analysis of SEM images, GROD maps, and KAM maps may reveal the most interesting locations for further FIB and TEM analyses [22].

3.4. Deformation-induced changes in the EBSD misorientation metrics

3.4.1. GROD as a function of plastic strain

The GROD value shows how one part of the grain is bent or rotated regarding the average grain orientation. High-GROD areas in the deformed material may be connected to inclusions or artificial defects [18,62]. Whereas GROD is not usually used to evaluate or quantify the strain level, this parameter may correlate well with the accumulated damage. For example, during fatigue or creep, the linear dependence between creep life and GROD was demonstrated in [18]. The linear relationship may be explained assuming that freshly appearing dislocations cross the grain body and accumulate near grain boundary. In the case of metallic material, grain boundaries are natural obstacles, at least at the small strain level. Strain transfer via grain boundary may occur as well, being a complex phenomenon [48,58], which depends on many factor including grain orientation and local grain configuration.

Figure 6 shows the maximum GROD value ($GROD_m$) observed within an ROI as a function of the local strain level. Here, the maximum GROD value, not an average one, was selected as an indicator of the plastic strain. This is not a common approach; however, the appearance of small local areas with a high GROD value is specific to the plastic strain mechanisms occurring in irradiated austenitic steels [22]. This mechanism may need a new way to be quantified and discussed. As follows from Figure 6, the $GROD_m$ value changed at a decreased rate and more smoothly in the nonirradiated steel. For the nonirradiated material, small strain increases led to small changes in the $GROD_m$, with a nearly linear relationship with strain level up to ~ 0.15 . Speculating, maximum GROD value may be roughly proportional to the dislocation density and strain level. At larger strains, high-angle boundaries that form inside grains lead to grain

fragmentation. For newly formed grains, their individual GROD values stopped increasing and saturated at $\sim 25^\circ$. That value may be a limit, beyond which internal grain structure will be rearranged to form an internal boundary or boundaries.

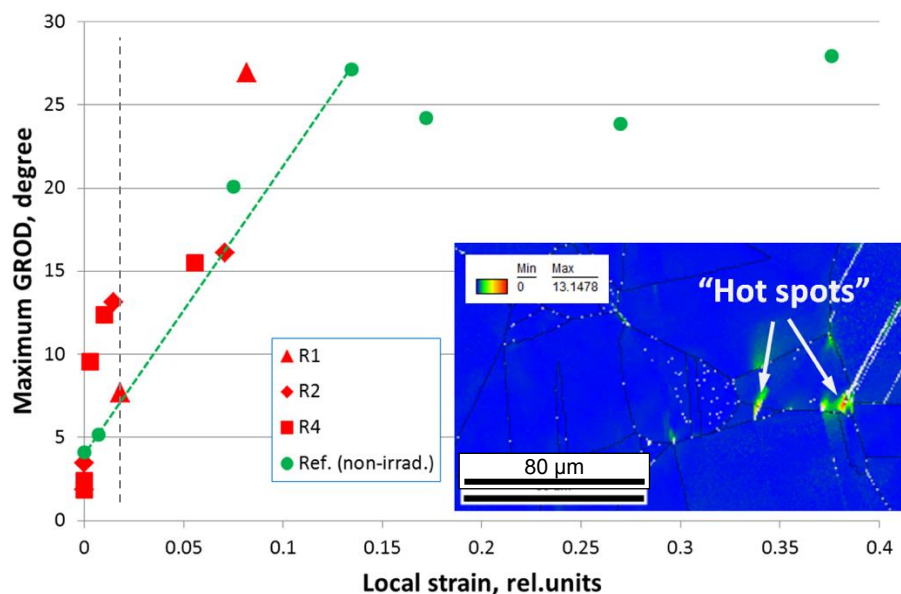


Figure 6. Maximum GROD value ($GROD_m$) observed within an EBSD scan as a function of the local plastic strain level. The vertical dashed line marked small strain area with a fast increase in $GROD_m$ value in the irradiated steel. Insertion shows a fragment of EBSD GROD map with several “hot spots.” Dashed line shows a data trend for the reference specimen to aid the reader.

Irradiated steel demonstrated a drastically different trend, compared with nonirradiated steel. Areas with high $GROD_m$ values appeared at small strains, suggesting high local strains and dislocation densities at the locations with increased $GROD_m$ values [22]. Data plotted for different ROIs (see Figure 6) do not follow the same trend but form a specific cloud of points well above the reference nonirradiated dataset. Thus, the local increase in $GROD_m$ value during deformation may be a stochastic process, which heavily depends on the local grain configuration. Limited information given in [22] suggests that the hot spot formation needs elastically “stiff” grains (oriented close to [111] or [101] with regard to the tensile direction) and an adjacent “soft” grain configuration (e.g., [001]).

A sudden increase in the $GROD_m$ value may be detected in the small strain area as a hot spot formation, but the further increase in strain as the in situ experiment progressed usually did not lead to a rapid increase in GROD value at the same location. Thus, the appearance of the hot spot may be a relaxation event, where local elastic stresses stimulate localized plastic deformation, generation of a large number of dislocations producing EBSD-visible orientation gradients, and other processes such as twinning [22]. In contrast to the nonirradiated steel, where dislocations

may move through the lattice more or less freely, radiation-induced defects within the grain limit the movement of dislocations to within a hot spot in an irradiated specimen. Thus, dislocations that accumulate in the vicinity of its origin point will produce high local misorientations.

Small-scale mechanical testing is a rapidly progressing research area. Specimens with gauge dimensions of several tens of microns may be produced using focused ion beams and subjected to tensile or compression testing [34,36,63]. This approach may be especially important for analyzing a broad range of damage doses and ion-irradiated specimens [34,63], and it is interesting to reproduce the hot spot phenomenon and study it in more details using micro-specimen approach. An obstacle here may be a scale factor if hot spots [22] appear only at large scale, in the objects consisting of tens or hundreds of grains.

3.4.2. Average KAM vs. plastic strain

The average KAM parameter and its modifications are often used to quantify plastic strain [3–5]. KAM does not rely directly on EBSD grain definition and thus is less sensitive to grain fragmentation than GROD. However, the KAM value depends on the EBSD step size and may be sensitive to the experimental conditions (e.g., specimen preparation and quality, voltage) [4].

Figure 7 average shows KAM value as a function of local plastic strain. For the reference material, KAM increased linearly up to a plastic strain value of ~0.2 to 0.25 and after that tended to saturate. This behavior agrees well with published data for nonirradiated austenitic steels of comparable composition; a linear relationship up to ~0.25 (~25%) of strain was reported in [4] and was shown to be independent on the EBSD system. A linear relationship for the true strain range of 0 to 0.25 was also observed in [64]. The increase in the average KAM value is caused by the accumulation of geometrically necessary dislocations in the structure, and average KAM value or another similar metric may be employed to measure the strain level via a calibration curve [4,64].

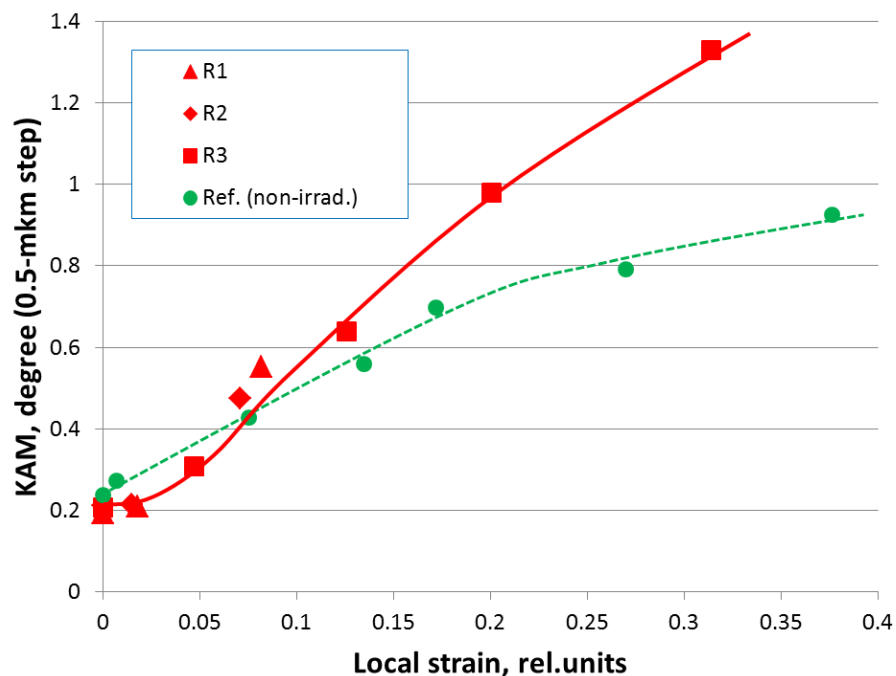


Figure 7. Average KAM as a function of the local plastic strain level for irradiated and reference specimens (step size = 0.5 μm). R1, R2, and R3: tracked ROIs. Lines show a polynomial fit to aid the reader.

KAM behavior for the irradiated steel is completely different (Figure 7). Weak, if any, changes in the average KAM value are measured up to strain level of ~ 0.03 . This result was unexpected since obvious plastic strain, and numerous slip lines (Figure 3) should have resulted in a dislocation density increase and increased KAM values. After a strain level of ~ 0.05 , the average KAM value started to grow at a much steeper slope than the value for the nonirradiated reference material. The results for several analyzed and tracked ROIs were pretty consistent, suggesting a two-stage kinetics with slow or zero increase in the KAM in the small strain area. Thus, a calibration curve obtained for reference nonirradiated material may not work after irradiation.

The observed trend for irradiated steel may be qualitatively explained as follows. Even at moderate strain levels (0.05-0.10), the structure of irradiated and deformed steel is a mix of virtually nondeformed parent material blocks interlaced with dislocation defect-free channels of ~ 40 to 50 nm width. An example may be seen in Figure 3d for $\sim 8.2\%$ local strain. At smaller strains, channel density is smaller, and the spacing between the channels is much higher. For most of the measured points, the electronic beam probes the nondeformed parent material, with very limited chance of hitting the deformed layer volume. Thus, most of the scanned area will be free, or almost free, of the strain-induced defects, resulting in very limited KAM change. Small local areas with increased KAM (Figure 4, 1.9% strain) will have a limited effect on the average KAM value. Thus, an approach based on the average KAM value may fail in revealing small plastic strains in irradiated material. Nevertheless, other data representation approaches (plotting

KAM maps or locating “hot spots” with high local GROD values) will easily reveal small plastic strain.

In the present work, the common EBSD approach that was employed provided the typical misorientation measurement error of $\sim 0.3^\circ$ to 0.5° for every point [4,5]. After KAM calculation, the noise level (or “floor level”) was $\sim 0.2^\circ$ to 0.3° . Smaller changes in the KAM (e.g., microplasticity or plastic deformation inside limited areas) are difficult to observe. To deal with small plastic strains, one may use special approaches such as KAM averaging along grain boundaries [1] or high-resolution EBSD [65].

3.5. EBSD assessment of deformation mechanisms in irradiated steel

Austenitic 300-series stainless steels may demonstrate multiple deformation mechanisms (e.g., twinning, phase instability, lattice rotation) during plastic straining depending on composition, deformation temperature, and irradiation [52,66]. The presence of second phases (for instance, delta-ferrite) also may influence strain-induced processes and misorientation evolution. Although a detailed study of these phenomena is not the intent of the present work, it was important to evaluate their visibility and accessibility via in situ SEM-EBSD analysis.

3.5.1. Second phase (retained bcc-ferrite) behavior

Figure 8 shows an EBSD dataset recorded at different strain levels. Few small retained ferrite particles were observed at this ROI prior to the test (R_f in Figure 8). Since the particles existed before straining, they may be easily distinguished from strain-induced martensite, which also has bcc-lattice. The observed ferrite may be either retained ferrite or an irradiation-induced phase [67,68]. EDS results (not shown) revealed that the ferrite particles were enriched in Cr and depleted in Ni, compared to the surrounding matrix. As plastic strain increased, areas with increased KAM value formed around the ferrite particles (see KAM_f -insertions in Figure 8); the particles appeared to serve as obstacles for dislocation motion. Interestingly, instead of the expected high strength, the ferrite particles also experienced plastic strain as local misorientation inside the particles strongly increased. Taking into account the close connection between stress corrosion crack initiation and localized strain [69,70], the role of ferrite in causing strain localization may become even more important. For instance, it was shown [71] that there is a direct correlation between the amount of magnetic phase (likely ferrite, but not confirmed in [71]) and irradiation-assisted stress corrosion cracking (IASCC) susceptibility.

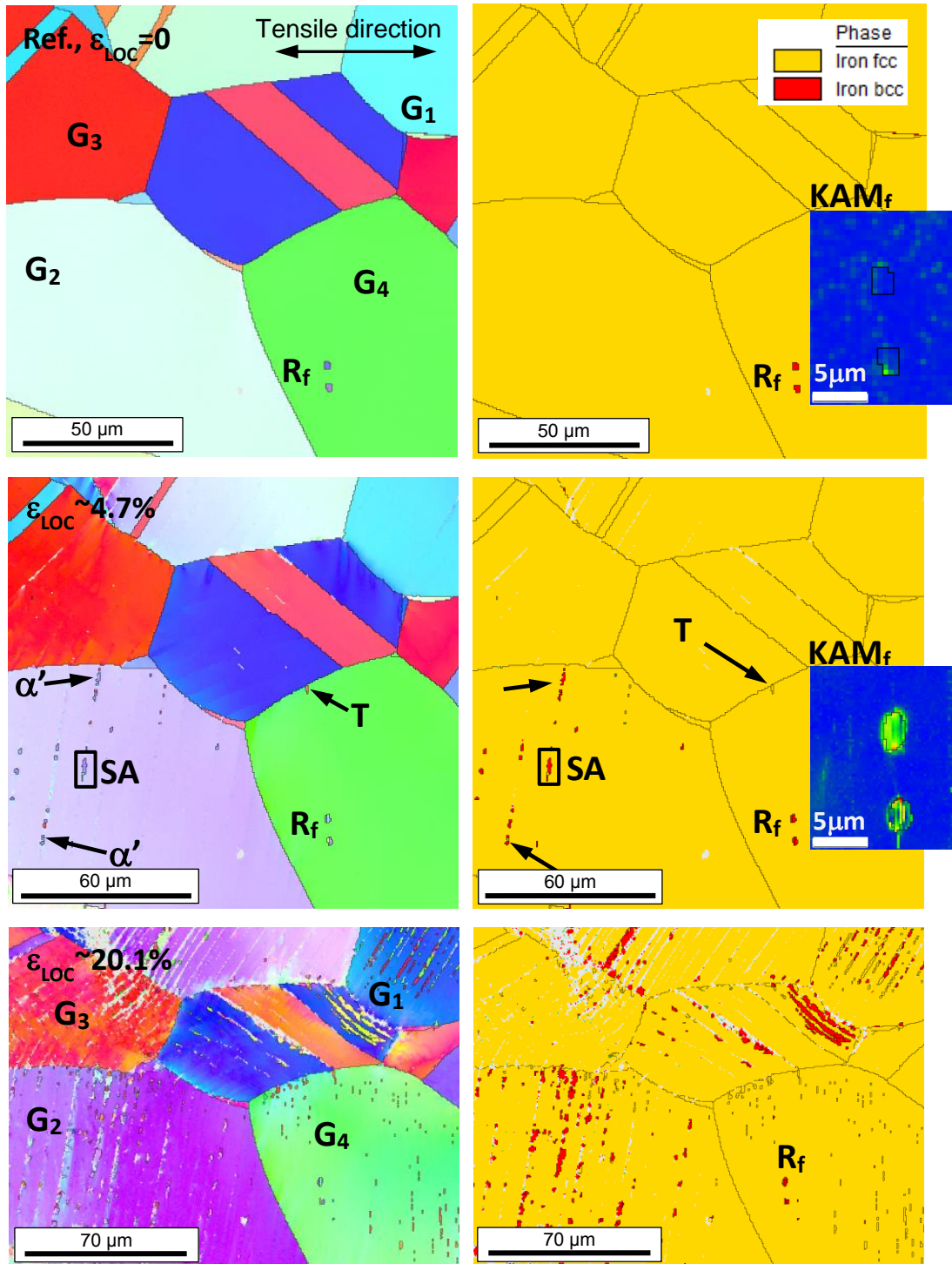


Figure 8. EBSD IPF and phase maps at different local strain levels (note, the scale bars are slightly different to compensate for plastic strain increase). T: fine deformation twin. R_f : small retained ferrite inclusions existed prior to the test; two insertions (KAM_f) present KAM value maps for these ferrite inclusions and the surrounding area before and after strain. Black arrows and α' -sign point the strain-induced α' -martensite domains formed along the defect-free

channels. G₁-G₄: grains with specific strain-induced phenomena (see details in the text). SA: subarea scanned with higher resolution and depicted in Figure 9.

3.5.2. Lattice rotation effects

The lattice rotation effects became evident as plastic strain increased (Figure 8). One may see the lattice rotation as a change of the grain color in the IPF maps. As the results show, austenitic lattice rotate toward the [001]-[111] line of the unit triangle (with respect to the tensile direction). For example, grains G₁ and G₂ with teal color prior the straining will “rotate” to the [111]-orientation changing color to light blue and blue. A small portion of the grains, usually areas adjacent to grain-boundaries, may demonstrate slightly different behavior, depending on the local stress and strain conditions [72,73]. Grains oriented close to [001] or [111] corners usually keep their orientation through the test (e.g., G₃ in Figure 8). This behavior is similar to the lattice rotation phenomena in nonirradiated fcc-metals and alloys [72,73]. Grains oriented close to [101] with respect to the tensile direction are supposed to rotate toward [111] but may retain their orientation long enough (e.g., G₄). Lattice rotation effects are crucial for plasticity modeling and will be addressed in detail in future work, using additional statistics.

3.5.3. Phase instability and twinning

Being especially pronounced at room temperature and below, twinning and phase instability are usually not considered as acting deformation mechanisms at elevated temperatures, such as that of light water reactor (LWR) service temperature. Nevertheless, twinning was observed in the neutron-irradiated austenitic steel at the LWR-relevant temperature [74], and phase transformation was found in J316 steel irradiated and tested at 330°C [52]. Recently, twinning and strain-induced martensite phases (α' and ϵ) were observed inside defect-free channels in 316L austenitic steel irradiated at high damage doses and deformed at LWR conditions [66].

In the current work, as the experiment progressed, and the specimen entered the elastic-plastic deformation mode, the EBSD maps revealed the appearance of new bcc domains, believed to be of martensitic origin. Elongated domains of bcc-phase (α' -martensite) became evident at the specimen surface at ~2% strain; no hcp (ϵ) martensite was reliably detected or confirmed via Kikuchi pattern analysis. The martensitic domains formed along dislocation channels as a specific chain- or hill-like formations with different contrast to the parent austenite (Figure 9a,b). No phase transformation was detected at the surface of the nonirradiated reference material up to the largest reached strain level (~35%). Specific phase transformation at the surface was observed by us earlier in 4.4-dpa neutron-irradiated 304L steel [43], with bcc-phase morphology studied using FIB-TEM. In the present work, at 20.1% of local strain, transformed domains reached a length of ~20 to 50 μm (Figure 8). Some grains (e.g., G₁, G₂ in Figure 8) appeared to be more transformed than others (G₃, G₄), suggesting strong grain orientation role.

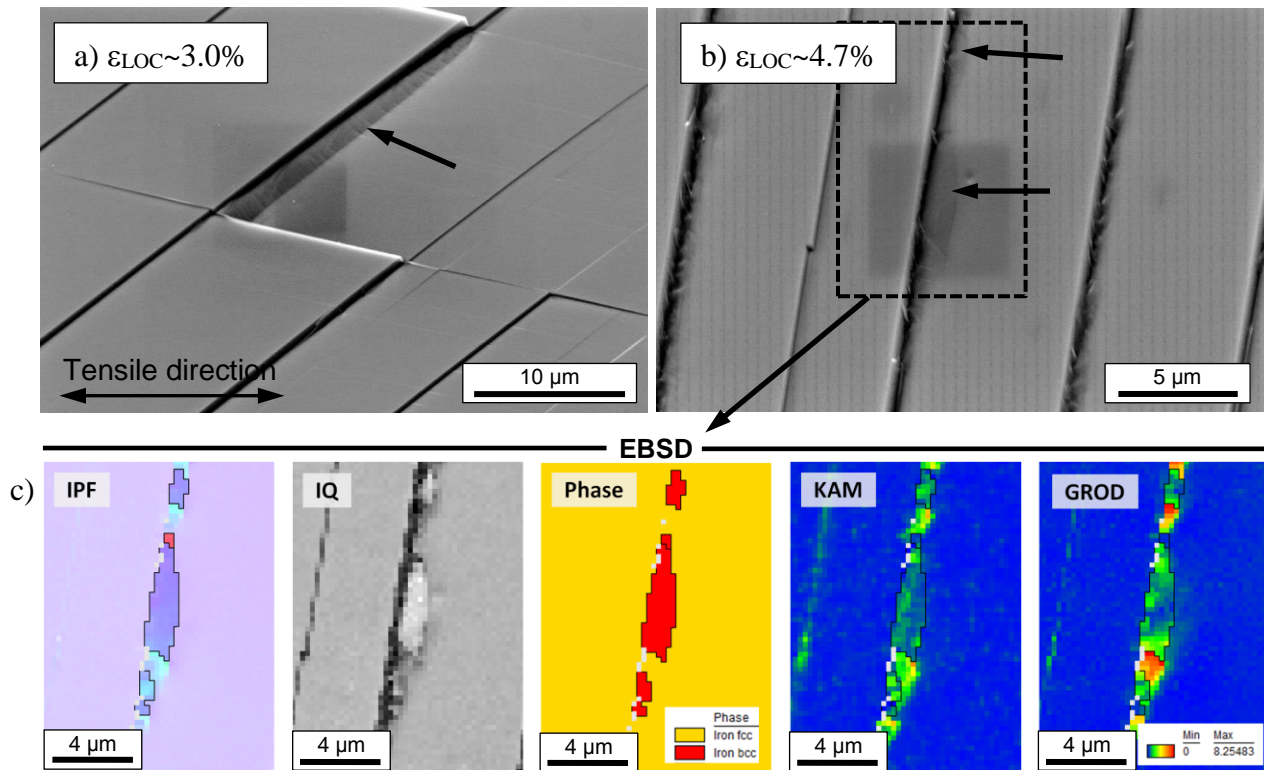


Figure 9. a, b) Transformed areas along the dislocation channels (SEM images are tilted 70°). The bcc domains are pointed by arrows; c) EBSD dataset for the area shown by the dashed rectangle in b) and designated as SA in Figure 8. In the phase map, austenite is yellow, bcc-martensite is red.

Several sub areas (e.g., SA in Figure 8) were scanned at high magnification and with a step size of 125 nm. Figure 9 shows α' -domain from the SA-subarea in Figure 8. The high-magnification scan revealed the complex structure of the transformed areas. The phase boundaries were clearly visible in the IQ map and provided a way to confirm the transformation event. The α' -particles formed chains, often interlacing with nontransformed austenite. The retained austenite between the α' -particles had very high KAM and GROD values and strong local misorientation gradients. These gradients suggest that transformation led to the appearance of highly localized plastic strain in the adjacent austenitic areas.

The transformed domains often appeared brighter in the IQ maps. This may be caused by surface orientation effect, but also may be evidence of different defect density inside the α' -particle compared to the parent austenite. Dislocation movement may “sweep out” radiation defects from the channel [22], but the impact of phase transformation on the preexisting radiation defects is not known. This observation – changes in IQ maps before and after transformation – requires additional attention in the future tests using recorded Kikuchi patterns.

Deformation twins were observed in scans performed with a 0.5 μm step starting at a strain level of $\sim 3\%$ to 5% . EBSD-resolvable twins were first observed, as a rule, near grain boundaries (see an example in Figure 8, 4.7% strain). At higher strains, the visible twins often appeared in the grain interior (grain G_4) and coexisted with strain-induced α' -phase (grain G_1 in Figure 8), forming specific chains where α' particles interlaced with deformation twins. The appearance of such structure raises an interesting question regarding what happens first: twin appearance with subsequent phase transformation inside newly formed twin or this line-like formation formed as a consequence of twinning and martensitic transformation events. Additional tests with smaller strain increments may be necessary to assess this aspect. The twinning intensity or, strictly speaking, the density and size of the visible twins, depends on grain orientation [75] with respect to the acting stress direction. The G_1 -grain (oriented close to $[111]$, as follows from the grain color) contains more twins (and twins are wider) than the G_4 -grain ($\sim 10^\circ$ from the $[101]$ orientation after $\sim 10\%$ strain), whereas no or very few twins are present in other grains.

Conventional EBSD may not resolve objects below some critical size. Very fine (i.e., $\sim 30\text{--}40$ nm) twins may present inside defect-free channels [43,74], but in situ testing with conventional SEM-EBSD analysis will miss such fine formations.

Figure 10 shows very specific twinning behavior. Twins are supposed to be thin (tens of nanometers) in the irradiated and deformed steel, but relatively large strain-induced objects ($\sim 1\text{--}2$ μm in width) of twinning origin were found. They were lighter in the IQ map, suggesting strongly reduced defect density. One may speculate that twin formation occurs outside the defect-free channels involving relatively large material volumes. An alternate explanation may be the presence of multiple, closely-located fine channels with internal twins; FIB-TEM analysis is necessary to answer this question. Wide twins were also observed in neutron-irradiated steels deformed in high-temperature water [76]; thus, this mechanism may be acting under NPP-relevant conditions.

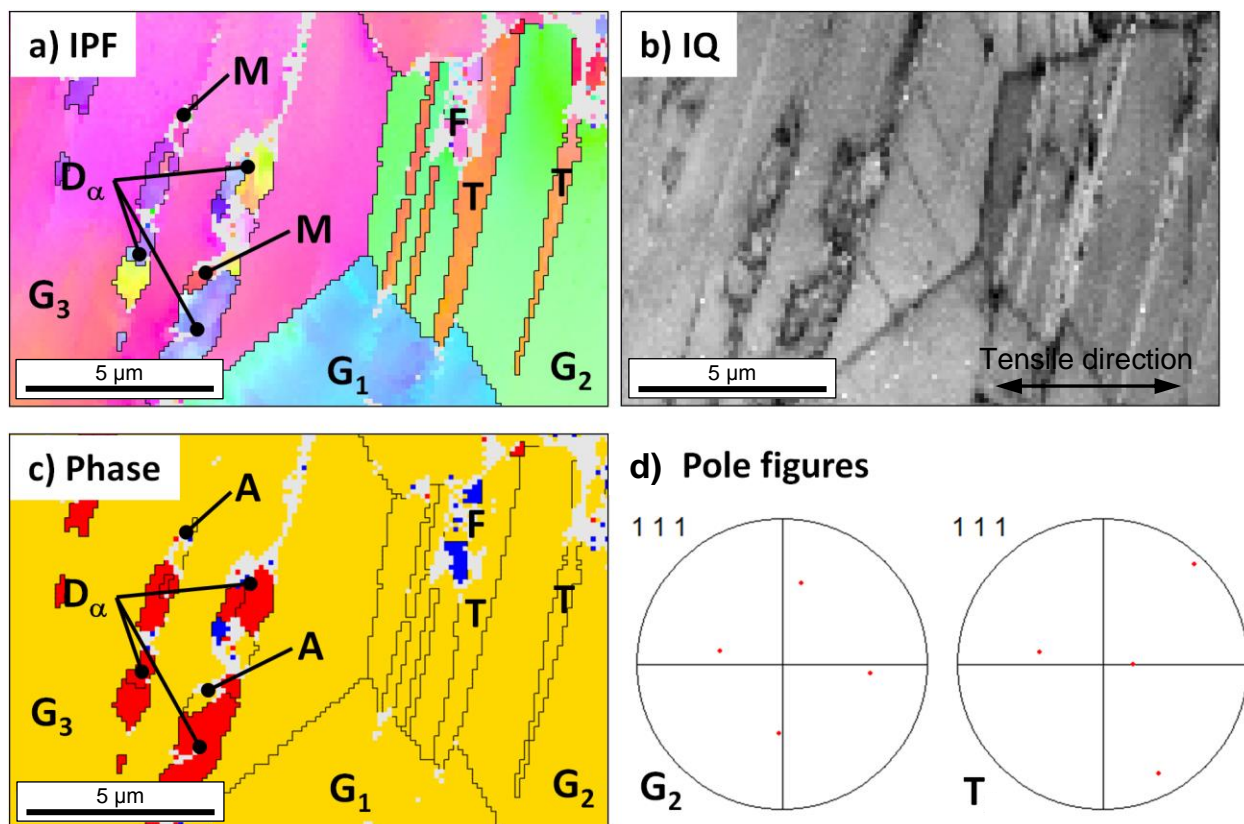


Figure 10. EBSD maps (a, b, c) for wide strain-induced twins (T) formed at moderate strain level (a local plastic strain of 8.2%). Pole figure (d) shows 60° rotation about one of the $\langle 111 \rangle$ -directions, confirming the twinning nature of the objects (T) in grain G₂. Grain G₁ has no signs of transformation events, whereas G₂ contains wide twins in contrast to the G₃ with martensitic domains only. D_α designates martensitic domains in the neighboring grain. EBSD step size is 125 nm. “F” shows false (not confirmed by recorded patterns) ϵ -phase indications.

It is interesting to use small-scale testing to investigate structure transformation events like the formation of the α' -domains shown in Figure 8 and Figure 9, or the wide twins in Figure 10 [34,36]. The domain size (a few micrometers) is close to that of a typical micro-scale specimen [34,36] and may allow for detailed study of these processes with particular focus on the role of grain orientation and the evolution of radiation defect structure.

Conclusions

The present work focused on microstructure evolution and misorientation evolution in irradiated austenitic steel during plastic deformation. Advanced in situ mechanical tests, accompanied by SEM-EBSD scanning were conducted using neutron-irradiated (5.9 dpa in boiling water reactor at 288°C) 304L steel specimens. Several selected ROIs were continuously scanned at different strain levels to track and analyze different strain-induced phenomena. The main focus was made on the misorientation evolution because very limited data exist at the moment for irradiated

steels; other processes, such as lattice rotation, twinning, and phase transformation, were discussed briefly to evaluate the potential of in situ SEM-EBSD testing in their assessment.

It was established that irradiation had a strong impact on KAM and GROD EBSD misorientation parameters. Thus, GROD maps revealed the formation of specific “hot spots” (areas with high local misorientation, up to 10° to 20°) in the small strain area (~ 0 – 0.02), in which the GROD value increased much more quickly in the irradiated steel than in the nonirradiated steel. In contrast, average KAM values showed very little overall changes (but strong localized increase inside the hot spots) in the strain range of ~ 0 to 0.02 ; after that, the average KAM values increased much more quickly in the irradiated steel than in the nonirradiated steel. It was concluded that local misorientation level increased in irradiated steel in a very localized fashion and significantly more quickly than it did in unirradiated steel.

Acknowledgments

The research was supported by the US Department of Energy, Office of Nuclear Energy, for the Light Water Reactor Sustainability Program research and development effort. Irradiated specimen manufacturing and in situ SEM-EBSD mechanical testing were performed at ORNL’s LAMDA laboratory; help and support of the LAMDA management and technical staff are greatly appreciated. The authors would like to thank Dr. P. Edmondson (ORNL) for help with developing and establishing the in situ testing approach at LAMDA, Dr. K. Field (ORNL) for reviewing the paper and valuable discussions, B. Eckhart and T. Dixon (ORNL) for help with specimen manufacturing, and W. Koncinski (ORNL) for help with manuscript preparation.

This manuscript has been authored by UT-Battelle, LLC under Contract No. DE-AC05-00OR22725 with the U.S. Department of Energy. The United States Government retains and the publisher, by accepting the article for publication, acknowledges that the United States Government retains a non-exclusive, paid-up, irrevocable, world-wide license to publish or reproduce the published form of this manuscript, or allow others to do so, for United States Government purposes. The Department of Energy will provide public access to these results of federally sponsored research in accordance with the DOE Public Access Plan (<http://energy.gov/downloads/doe-public-access-plan>).

References

- [1] K. Fukuya, H. Nishioka, K. Fujii, T. Miura, and Y. Kitsunai, “Local strain distribution near grain boundaries under tensile stresses in highly irradiated SUS316 stainless steel,” *Journal of Nuclear Materials*, vol. 432, 2013, pp. 67–71.
- [2] J. Hou, T. Shoji, Z.P. Lu, Q. Peng, J. Wang, E.-H. Han, and W. Ke, “Residual strain measurement and grain boundary characterization in the heat-affected zone of a weld joint

- between Alloy 690TT and Alloy 52,” *Journal of Nuclear Materials*, vol. 397, 2010, pp. 109–115.
- [3] M. Kamaya, “Assessment of local deformation using EBSD: Quantification of local damage at grain boundaries,” *Materials characterization*, vol. 66, 2012, pp. 56–67.
- [4] M. Kamaya, K. Kubushiro, Y. Sakakibara, S. Suzuki, H. Morita, R. Yoda, D. Kobayashi, K. Yamagiwa, T. Nishioka, Y. Yamazaki, and others, “Round robin crystal orientation measurement using EBSD for damage assessment,” *Mechanical Engineering Journal*, vol. 3, 2016, pp. 16–77.
- [5] M. Kamaya, A.J. Wilkinson, and J.M. Titchmarsh, “Quantification of plastic strain of stainless steel and nickel alloy by electron backscatter diffraction,” *Acta Materialia*, vol. 54, 2006, pp. 539–548.
- [6] T. Liu, S. Xia, Q. Bai, B. Zhou, L. Zhang, Y. Lu, and T. Shoji, “Three-dimensional study of grain boundary engineering effects on intergranular stress corrosion cracking of 316 stainless steel in high temperature water,” *Journal of Nuclear Materials*, vol. 498, 2018, pp. 290–299.
- [7] M. McMurtrey, G. Was, L. Patrick, and D. Farkas, “Relationship between localized strain and irradiation assisted stress corrosion cracking in an austenitic alloy,” *Materials Science and Engineering: A*, vol. 528, 2011, pp. 3730–3740.
- [8] A. Sáez-Maderuelo, L. Castro, and G. de Diego, “Plastic strain characterization in austenitic stainless steels and nickel alloys by electron backscatter diffraction,” *Journal of Nuclear Materials*, vol. 416, 2011, pp. 75–79.
- [9] S.I. Wright, M.M. Nowell, and D.P. Field, “A review of strain analysis using electron backscatter diffraction,” *Microscopy and microanalysis*, vol. 17, 2011, pp. 316–329.
- [10] M. Calcagnotto, D. Ponge, E. Demir, and D. Raabe, “Orientation gradients and geometrically necessary dislocations in ultrafine grained dual-phase steels studied by 2D and 3D EBSD,” *Materials Science and Engineering: A*, vol. 527, 2010, pp. 2738–2746.
- [11] K. Thomsen, K. Mehnert, P.W. Trimby, and A. Gholinia, “Quaternion-based disorientation coloring of orientation maps,” *Ultramicroscopy*, vol. 182, 2017, pp. 62–67.
- [12] R.R. Shen, V. Ström, and P. Efsing, “Spatial correlation between local misorientations and nanoindentation hardness in nickel-base alloy 690,” *Materials Science and Engineering: A*, vol. 674, 2016, pp. 171–177.
- [13] T.M. Angeliu, E.L. Hall, J. Sutliff, S. Sitzmen, P.L. Andresen, and others, “Strain and microstructure characterization of austenitic stainless steel weld HAZs,” *CORROSION 2000*, NACE International, 2000.
- [14] E.M. Lehigh, Y.-P. Lin, and O.E. Lepik, “Mapping residual plastic strain in materials using electron backscatter diffraction,” *Electron backscatter diffraction in materials science*, Springer, 2000, pp. 247–264.
- [15] J. Sutliff, “An investigation of plastic strain in copper by automated-EBSD,” *Microsc. Microanal.*, vol. 2, 1999, pp. 236–237.
- [16] C. Blochwitz, J. Brechbühl, and W. Tirschler, “Analysis of activated slip systems in fatigue nickel polycrystals using the EBSD-technique in the scanning electron microscope,” *Materials Science and Engineering: A*, vol. 210, 1996, pp. 42–47.
- [17] M. Kamaya and M. Kuroda, “Fatigue damage evaluation using electron backscatter diffraction,” *Materials transactions*, vol. 52, 2011, pp. 1168–1176.

- [18] D. Kobayashi, M. Miyabe, Y. Kagiya, Y. Nagumo, R. Sugiura, T. Matsuzaki, and A.T. Yokobori, "Geometrical influence for creep damage evaluation of IN738LC using electron backscatter diffraction," *Materials at High Temperatures*, vol. 29, 2012, pp. 301–307.
- [19] K. Mino, R. Imamura, H. Koiwai, and C. Fukuoka, "Residual life prediction of turbine blades of aeroderivative gas turbines," *Advanced Engineering Materials*, vol. 3, 2001, pp. 922–924.
- [20] R. Yoda, T. Yokomaku, and N. Tsuji, "Plastic deformation and creep damage evaluations of type 316 austenitic stainless steels by EBSD," *Materials characterization*, vol. 61, 2010, pp. 913–922.
- [21] G.S. Was, Y. Ashida, and P.L. Andresen, "Irradiation-assisted stress corrosion cracking," *Corrosion Reviews*, vol. 29, 2011, pp. 7–49.
- [22] K.G. Field, M.N. Gussev, and J.T. Busby, "Microstructural characterization of deformation localization at small strains in a neutron-irradiated 304 stainless steel," *Journal of Nuclear Materials*, vol. 452, 2014, pp. 500–508.
- [23] K. Lambrinou, E. Charalampopoulou, T.V. der Donck, R. Delville, and D. Schryvers, "Dissolution corrosion of 316L austenitic stainless steels in contact with static liquid lead-bismuth eutectic (LBE) at 500 °C," *Journal of Nuclear Materials*, vol. 490, 2017, pp. 9–27.
- [24] H. Borkar, S. Seifeddine, and A.E.W. Jarfors, "In-situ EBSD study of deformation behavior of Al–Si–Cu alloys during tensile testing," *Materials & Design*, vol. 84, 2015, pp. 36–47.
- [25] C. Caër and R. Pesci, "Local behavior of an AISI 304 stainless steel submitted to in situ biaxial loading in SEM," *Materials Science and Engineering: A*, vol. 690, 2017, pp. 44–51.
- [26] S. Chakrabarty, S.K. Mishra, and P. Pant, "Crystallographic orientation and boundary effects on misorientation development in austenitic stainless steel," *Materials Science and Engineering: A*, vol. 617, 2014, pp. 228–234.
- [27] Y.B. Das, A.N. Forsey, T.H. Simm, K.M. Perkins, M.E. Fitzpatrick, S. Gungor, and R.J. Moat, "In situ observation of strain and phase transformation in plastically deformed 301 austenitic stainless steel," *Materials & Design*, vol. 112, 2016, pp. 107–116.
- [28] T. Fukino, S. Tsurekawa, and Y. Morizono, "In-situ scanning electron microscopy/electron backscattered diffraction observation of microstructural evolution during $\alpha \rightarrow \gamma$ phase transformation in deformed Fe-Ni alloy," *Metallurgical and Materials Transactions A*, vol. 42, 2011, pp. 587–593.
- [29] A. Järvenpää, M. Jaskari, J. Man, and L.P. Karjalainen, "Austenite stability in reversion-treated structures of a 301LN steel under tensile loading," *Materials Characterization*, vol. 127, 2017, pp. 12–26.
- [30] W. Wang, T. Liu, X. Cao, Y. Lu, and T. Shoji, "In-situ observation on twin boundary evolution and crack initiation behavior during tensile test on 316L austenitic stainless steel," *Materials Characterization*, vol. 132, 2017, pp. 169–174.
- [31] F. Latourte, T. Salez, A. Guery, N. Rupin, and M. Mahé, "Deformation studies from in situ SEM experiments of a reactor pressure vessel steel at room and low temperatures," *Journal of Nuclear Materials*, vol. 454, 2014, pp. 373–380.
- [32] J. Gupta, J. Hure, B. Tanguy, L. Laffont, M.-C. Lafont, and E. Andrieu, "Characterization of ion irradiation effects on the microstructure, hardness, deformation and crack initiation behavior of austenitic stainless steel: Heavy ions vs protons," *Journal of Nuclear Materials*, vol. 501, 2018, pp. 45–58.

- [33] M. Gussev, J. Busby, and F. Garner, "Phase instability and martensitic transformation as a potential degradation mode of nuclear plant internal components," *17th International Conference on Environmental Degradation of Materials in Nuclear Power Systems—Water Reactors*, 2015.
- [34] C. Howard, C.D. Judge, D. Poff, S. Parker, M. Griffiths, and P. Hosemann, "A novel in-situ, lift-out, three-point bend technique to quantify the mechanical properties of an ex-service neutron irradiated inconel X-750 component," *Journal of Nuclear Materials*, vol. 498, 2018, pp. 149–158.
- [35] K.J. Leonard, M.N. Gussev, J.N. Stevens, and J.T. Busby, "Analysis of stress corrosion cracking in alloy 718 following commercial reactor exposure," *Journal of Nuclear Materials*, vol. 466, 2015, pp. 443–459.
- [36] H.T. Vo, A. Reichardt, D. Frazer, N. Bailey, P. Chou, and P. Hosemann, "In situ micro-tensile testing on proton beam-irradiated stainless steel," *Journal of Nuclear Materials*, vol. 493, 2017, pp. 336–342.
- [37] W. Karlsen, J. Pakarinen, A. Toivonen, and U. Ehrnstén, "Deformation microstructures of 30 dpa AISI 304 stainless steel after monotonic tensile and constant load autoclave testing," *Proceedings of the 15th International Conference on Environmental Degradation of Materials in Nuclear Power Systems—Water Reactors*, Springer, 2011, pp. 1429–1446.
- [38] M. Sauzay, K. Bavard, and W. Karlsen, "TEM observations and finite element modelling of channel deformation in pre-irradiated austenitic stainless steels—Interactions with free surfaces and grain boundaries," *Journal of Nuclear Materials*, vol. 406, 2010, pp. 152–165.
- [39] A. Jenssen, "Machining and Shipment of Specimens from Heat SW – Documentation of Fabricated Specimens," *Report N13/210, Job No.211028, Studsvik Nuclear AB*, 2013.
- [40] Z. Jiao, J. Hesterberg, and G.S. Was, "Effect of post-irradiation annealing on the irradiated microstructure of neutron-irradiated 304L stainless steel," *Journal of Nuclear Materials*, vol. 500, 2018, pp. 220–234.
- [41] M. Gussev, J. Busby, K. Field, M. Sokolov, and S. Gray, "Role of scale factor during tensile testing of small specimens," *Small Specimen Test Techniques: 6th Volume*, ASTM International, 2015.
- [42] M. Gussev, P. Edmondson, and K. Leonard, "Beam current effect as a potential challenge in SEM-EBSD in situ tensile testing," *Materials Characterization*, 2018.
- [43] M.N. Gussev, K.G. Field, and J.T. Busby, "Strain-induced phase transformation at the surface of an AISI-304 stainless steel irradiated to 4.4 dpa and deformed to 0.8% strain," *Journal of Nuclear Materials*, vol. 446, 2014, pp. 187–192.
- [44] S. Kahl, R.L. Peng, M. Calmunger, B. Olsson, and S. Johansson, "In situ EBSD during tensile test of aluminum AA3003 sheet," *Micron*, vol. 58, 2014, pp. 15–24.
- [45] G. Nolze, "Image distortions in SEM and their influences on EBSD measurements," *Ultramicroscopy*, vol. 107, 2007, pp. 172–183.
- [46] K. Hariharan, P. Dubey, and J. Jain, "Time dependent ductility improvement of stainless steel SS 316 using stress relaxation," *Materials Science and Engineering: A*, vol. 673, 2016, pp. 250–256.
- [47] A. Causey, G. Carpenter, and S. MacEwen, "In-reactor stress relaxation of selected metals and alloys at low temperatures," *Journal of Nuclear Materials*, vol. 90, 1980, pp. 216–223.
- [48] Z. Jiao and G. Was, "Impact of localized deformation on IASCC in austenitic stainless steels," *Journal of Nuclear Materials*, vol. 408, 2011, pp. 246–256.

- [49] Z. Jiao, G. Was, T. Miura, and K. Fukuya, "Aspects of ion irradiations to study localized deformation in austenitic stainless steels," *Journal of Nuclear Materials*, vol. 452, 2014, pp. 328–334.
- [50] D.C. Johnson, B. Kuhr, D. Farkas, and G.S. Was, "Quantitative analysis of localized stresses in irradiated stainless steels using high resolution electron backscatter diffraction and molecular dynamics modeling," *Scripta Materialia*, vol. 116, 2016, pp. 87–90.
- [51] Z. Jiao, "Influence of localized deformation on irradiation-assisted stress corrosion cracking of proton-irradiated austenitic alloys," *Proc. 12th Int. Conf. on Environmental Degradation of Materials in Nuclear Power Systems-Water Reactors, 2005*, TMS, 2005.
- [52] A. Hojná, "Overview of Intergranular Fracture of Neutron Irradiated Austenitic Stainless Steels," *Metals*, vol. 7, 2017, p. 392.
- [53] J. Kacher and I. Robertson, "Quasi-four-dimensional analysis of dislocation interactions with grain boundaries in 304 stainless steel," *Acta Materialia*, vol. 60, 2012, pp. 6657–6672.
- [54] A. Arsenlis, M. Rhee, G. Hommes, R. Cook, and J. Marian, "A dislocation dynamics study of the transition from homogeneous to heterogeneous deformation in irradiated body-centered cubic iron," *Acta Materialia*, vol. 60, 2012, pp. 3748–3757.
- [55] A. Patra and D.L. McDowell, "Continuum modeling of localized deformation in irradiated bcc materials," *Journal of Nuclear Materials*, vol. 432, 2013, pp. 414–427.
- [56] X. Zhao, D.J. Strickland, P.M. Derlet, M. He, Y.-J. Cheng, J. Pu, K. Hattar, and D.S. Gianola, "In situ measurements of a homogeneous to heterogeneous transition in the plastic response of ion-irradiated $\langle 111 \rangle$ Ni microspecimens," *Acta Materialia*, vol. 88, 2015, pp. 121–135.
- [57] D. Dingley, "Progressive steps in the development of electron backscatter diffraction and orientation imaging microscopy," *Journal of microscopy*, vol. 213, 2004, pp. 214–224.
- [58] M.N. Gussev, K.G. Field, and J.T. Busby, "Deformation localization and dislocation channel dynamics in neutron-irradiated austenitic stainless steels," *Journal of Nuclear Materials*, vol. 460, 2015, pp. 139–152.
- [59] C. Haase, M. Kühbach, L.A. Barrales-Mora, S.L. Wong, F. Roters, D.A. Molodov, and G. Gottstein, "Recrystallization behavior of a high-manganese steel: Experiments and simulations," *Acta Materialia*, vol. 100, 2015, pp. 155–168.
- [60] S.S.S. Kumar, T. Raghu, P.P. Bhattacharjee, G.A. Rao, and U. Borah, "Work hardening characteristics and microstructural evolution during hot deformation of a nickel superalloy at moderate strain rates," *Journal of Alloys and Compounds*, vol. 709, 2017, pp. 394–409.
- [61] M.P. Echlin, M.S. Titus, M. Straw, P. Gumbsch, and T.M. Pollock, "Materials response to glancing incidence femtosecond laser ablation," *Acta Materialia*, vol. 124, 2017, pp. 37–46.
- [62] S. Kobayashi, C. Zambaldi, and D. Raabe, "Orientation dependence of local lattice rotations at precipitates: Example of κ -Fe₃AlC carbides in a Fe₃Al-based alloy," *Acta Materialia*, vol. 58, 2010, pp. 6672–6684.
- [63] T. Miura, K. Fujii, and K. Fukuya, "Micro-mechanical investigation for effects of helium on grain boundary fracture of austenitic stainless steel," *Journal of Nuclear Materials*, vol. 457, 2015, pp. 279–290.
- [64] D.N. Githinji, S.M. Northover, P.J. Bouchard, and M.A. Rist, "An EBSD study of the deformation of service-aged 316 austenitic steel," *Metallurgical and Materials Transactions A*, vol. 44, 2013, pp. 4150–4167.

- [65] T.B. Britton, J. Jiang, R. Clough, E. Tarleton, A.I. Kirkland, and A.J. Wilkinson, "Assessing the precision of strain measurements using electron backscatter diffraction – part 1: Detector assessment," *Ultramicroscopy*, vol. 135, 2013, pp. 126–135.
- [66] A. Renault-Laborne, J. Hure, J. Malaplate, P. Gavoille, F. Sefta, and B. Tanguy, "Tensile properties and deformation microstructure of highly neutron-irradiated 316 stainless steels at low and fast strain rate," *Journal of Nuclear Materials*, 2018.
- [67] M.N. Gussev, J.T. Busby, L. Tan, and F.A. Garner, "Magnetic phase formation in irradiated austenitic alloys," *Journal of Nuclear Materials*, vol. 448, 2014, pp. 294–300.
- [68] D. Porter, "Ferrite formation in neutron-irradiated type 304L stainless steel," *Journal of Nuclear Materials*, vol. 79, 1979, pp. 406–411.
- [69] W. Karlsen, G. Diego, and B. Devrient, "Localized deformation as a key precursor to initiation of intergranular stress corrosion cracking of austenitic stainless steels employed in nuclear power plants," *Journal of Nuclear Materials*, vol. 406, 2010, pp. 138–151.
- [70] G.S. Was, D. Farkas, and I.M. Robertson, "Micromechanics of dislocation channeling in intergranular stress corrosion crack nucleation," *Current Opinion in Solid State and Materials Science*, vol. 16, 2012, pp. 134–142.
- [71] S. Takaya, Y. Nagae, T. Yoshitake, Y. Nemoto, J. Nakano, F. Ueno, K. Aoto, and T. Tsukada, "Examination of relation between IASCC susceptibility and magnetic property," *E-Journal of Advanced Maintenance*, vol. 1, 2009, pp. 44–51.
- [72] P. Chen, S.C. Mao, Y. Liu, F. Wang, Y.F. Zhang, Z. Zhang, and X.D. Han, "In-situ EBSD study of the active slip systems and lattice rotation behavior of surface grains in aluminum alloy during tensile deformation," *Materials Science and Engineering: A*, vol. 580, 2013, pp. 114–124.
- [73] G. Winther, L. Margulies, S. Schmidt, and H. Poulsen, "Lattice rotations of individual bulk grains Part II: correlation with initial orientation and model comparison," *Acta Materialia*, vol. 52, 2004, pp. 2863–2872.
- [74] T. Onchi, K. Dohi, N. Soneda, J. Cowan, R. Scowen, and M. Castano, "Fractographic and microstructural characterization of irradiated 304 stainless steel intergranularly fractured in inert gas," *Journal of nuclear materials*, vol. 320, 2003, pp. 194–208.
- [75] M.N. Gussev, J.T. Busby, T.S. Byun, and C.M. Parish, "Twinning and martensitic transformations in nickel-enriched 304 austenitic steel during tensile and indentation deformations," *Materials Science and Engineering: A*, vol. 588, 2013, pp. 299–307.
- [76] M.N. Gussev, K.G. Field, J.T. Busby, and K.J. Leonard, *Post-deformation examination of specimens subjected to SCC testing*, Oak Ridge National Laboratory (ORNL), Oak Ridge, TN (United States), 2016.